Editors' Suggestion

Local chromatic correction optics for Future Circular Collider e^+e^-

Pantaleo Raimondi*
Fermilab, Batavia, Illinois 60510, USA

Simone Maria Liuzzo,† Laurent Farvacque, and Simon White
ESRF, Grenoble, France

Michael Hofer
CERN, Geneva, Switzerland

(Received 18 October 2024; accepted 22 January 2025; published 13 February 2025)

Local chromatic correction optics are proposed for the Future Circular $e^+ - e^-$ Collider. These new optics assume an identical layout of the magnets at all operation energies and include a new design for the arcs, for the straight sections, and for the final focus. The arcs design is a step forward from the classic FODO lattice that achieves near cancellation up to the fourth order of chromatic and geometric aberrations. Straight sections and the final focus benefit from the application of transparency conditions and are thus minimally impacting the global beam dynamics. The final focus design includes both vertical and horizontal chromaticity correction sections, crab sextupoles, and additional specific sextupoles and decapoles for the optimization of the dynamics off-energy. Decapoles are very effective in mitigating the reduction of dynamic aperture due to synchrotron radiation. Nonlinear magnet settings are further optimized with multiobjective algorithms. The overall properties of the new optics proposed are analyzed in the presence of errors and compared to other optics designs.

DOI: 10.1103/PhysRevAccelBeams.28.021002

I. INTRODUCTION

The Future Circular Collider (FCC) project [1] is being evaluated as the next high-energy collider for the international community, targeting precision Higgs boson Physics and tests of the standard model. The FCC project has several steps of implementation to exploit at most the use of the ∼91 km tunnel required for its construction. The first stage is represented by an electron positron collider (FCC-ee), to be operated at the center of mass energies corresponding to the production of Z bosons (45.6 GeV), W bosons, Higgs bosons (125 GeV), and $t\bar{t}$ quark pairs (182.5 GeV). The present electron beam optics of the FCC-ee collider, named Global Hybrid chromaticity Correction (GHC) optics, are detailed in [2] and available in a dedicated repository [3]. The optics proposed in this paper, called henceforth local chromatic correction (LCC) optics, present several advantages compared to the optics in [2,3]: strongly improved beam dynamics off-axis and off-energy, reduced energy loss per turn, and weaker magnetic strengths. The arcs of the LCC optics are designed with techniques used for the design of synchrotron radiation (SR) light sources [4,5]. The final focus (FF) design is an evolution of the SuperB [6] design with many features specifically developed for FCC-ee. For example, a novel technique was developed to reduce detrimental effects induced by synchrotron radiation from the interaction region quadrupoles. In the later section, the design choices and the properties of the LCC lattice optics are detailed.

Section II introduces the optics design strategy.

Sections III, IV, and V detail the design choices for the arcs long straight sections (LSS), and the final focus, respectively.

Section VI describes the optimizations of nonlinear optics with numerical algorithms.

Sections VII and VIII detail the lattice properties and sensitivity to errors.

II. OPTICS DESIGN STRATEGY

The optics design aims to achieve the highest possible degree of *achromaticity* and *anharmonicity*. Moreover, chromaticities and transverse nonlinearities are compensated as locally as possible. This approach presents several advantages: minimization of the absolute value of the

*Contact author: praimond@fnal.gov
†Contact author: simone.liuzzo@esrf.fr

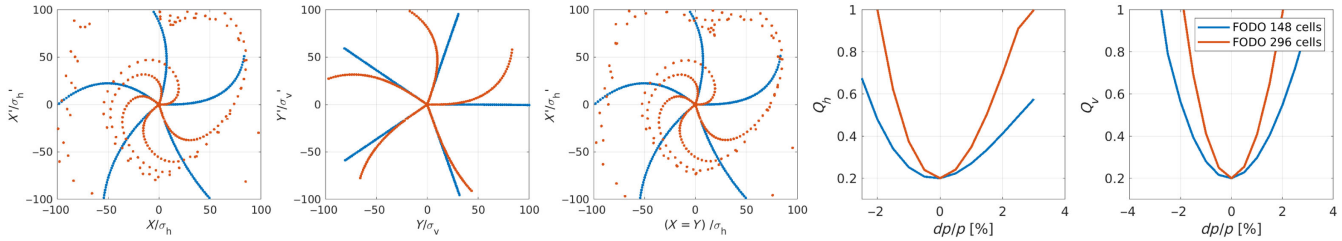

FIG. 1. Coordinates at each of five turns tracking particles starting on the horizontal axis (first plot on the left), vertical axis (second plot from the left), and for particles with identical horizontal and vertical coordinates (third plot from the left). The fourth and fifth plots show horizontal and vertical detuning with momentum. The curves refer to two FODO arc lattice options with phase advance $(\mu_h, \mu_v) = (90, 90)$ deg: 148 cells (Z) and 296 cells ($t\bar{t}$). These are used by the GHC optics and utilize noninterleaved sextupoles pairs at $-\mathcal{I}$.

resonance driving terms [7] and Montague functions [8]; reduced sensitivity of nonlinear cancellations to errors; orthogonal cancellation of aberrations; and the creation of orthogonal tuning knobs. A lattice is considered *achromatic* if the variation of the main optics parameters, such as the tunes and the optics ($\beta^*_{h,v}$, $\alpha^*_{h,v}$) at the interaction point (IP), has a small dependency on the variation of energy in a range as large as possible, ideally above 2% at Z and 3% at $t\bar{t}$ energy [9–11]. Similarly, a lattice is *anharmonic* when transverse dynamics scale linearly with respect to x and y actions. To evaluate *achromaticity* and *anharmonicity,* given lattice figures such as Fig. 1 are produced. The *"starfish"* plots on the left side of Fig. 1 show the tracking for particles at increasing initial transverse offset horizontally, vertically, or diagonally ($X = Y$). The tracking is performed for five turns only, and for better clarity, the tunes are set far from 0 and 0.5: $(Q_h, Q_v) = (0.2, 0.3)$ to produce five straight lines in phase space. For large amplitude, the nonlinear contributions transform the initial coordinates distributed onto a straight line into a curve with nonzero second and higher order polynomial components. The more a lattice is *anharmonic,* the more the coordinates at each of the five turns will be close to straight lines. A *"quasi time-independent"* motion is achieved by seeking a solution where the particles after five turns return to the original coordinates. This is very significant because a time-independent motion corresponds to stable particles and provides a quick insight into the extent of the DA.

Achromaticity is instead visualized by the standard detuning with momentum when chromaticities are set to $(\xi_h, \xi_v) = (0.0, 0.0)$ as in the right plots of Fig. 1. Higher order amplitude detuning coefficients ($\partial^n Q_{h,v}/\partial^n x$, $\partial^n Q_{h,v}/\partial^n y$, $\partial^n Q_{h,v}/\partial^n (x = y)$) are minimized to achieve *anharmonicity.* High-order detuning coefficients $\partial^n Q_{h,v}/\partial^n \delta$ close to zero make the lattice nearly *achromatic*. Starfish plots produce a quick snapshot of the combined effects of high-order amplitude and energy detuning coefficients on transverse beam dynamics. Throughout the present work, they are used as a global and fast observable for all high-order effects.

A crucial aspect of the design of a collider is the ability to insert sections with minimum impact on the overall ring performances with respect to arc-only performances. This is achieved by using the *transparency condition* (TC) described in [5] and reported later in Sec. IV A.

The design of the final focus (FF) system does not rely on the arc sextupoles to correct the chromaticity of the low β insertions. This allows maximal margins for dynamic aperture (DA) and momentum acceptance (MA) optimization. The FF is treated as an insertion in the ring that meets the transparency conditions just as any other section inserted in the optics.

Several methodologies and solutions are adopted to accommodate all the necessary lattice requirements as defined in the FCC-ee Conceptual Design Report (CDR) [1], such as general ring layout, crossing angle at the IP, straight sections length, parasitic crossing, rf, injection region, and arcs distance between e^+ and e^- rings, with

TABLE I. Full-ring general parameters for the two energies considered.

	Z	$t\bar{t}$
C (km)	90.659	90.659
Energy (GeV)	45.6	182.5
Number of IP per ring	4	4
Crossing angle (mrad)	30	30
Betatron tunes	(198.26, 174.38)	(350.224, 266.36)
Chromaticity	(0.20, 0.21)	(0.23, 1.66)
ϵ_h (pm rad)	684.72	2100.9
J	(1, 1, 2)	(1, 1, 2)
α_c	2.894×10^{-5}	0.946×10^{-5}
U_0 (MeV/turn)	34.3	8808.2
σ_E	3.715×10^{-4}	14.9×10^{-4}
β^*_v (mm)	0.7	1.6
β^*_h (mm)	100	1000
Bunch length (mm)	3.4	2.7
rf Voltage (GV)	0.17	10.4
rf frequency (MHz)	400	400
Long. damping time (ms)	401.6	6.3
Synchrotron tune	0.045	0.074

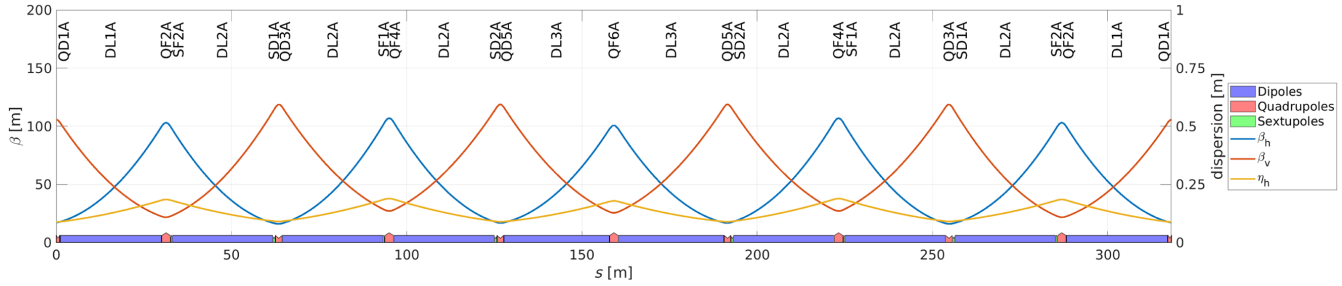

FIG. 2. HFD arc cell optics at $t\bar{t}$ and magnet families naming convention.

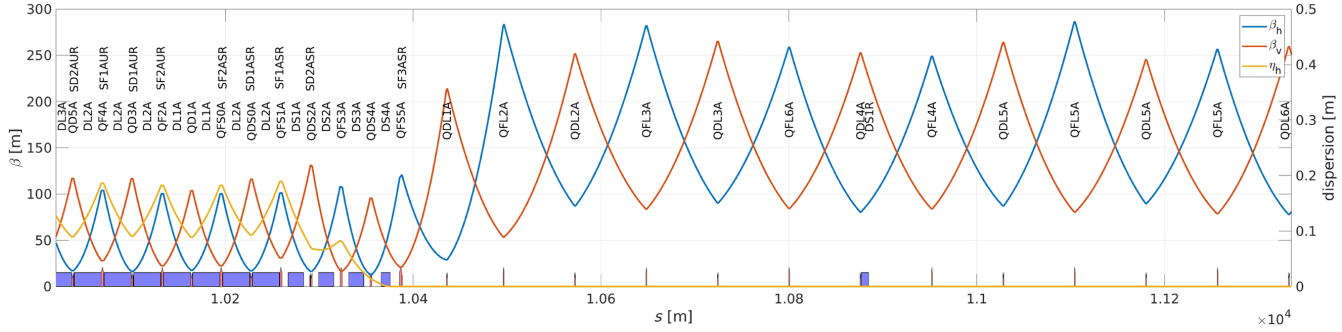

FIG. 3. Half long straight section. The last four dipoles are halved to suppress dispersion. The quadrupoles and sextupoles adjacent to the LSS on both sides are also tuned for on- and off-energy optics optimization.

minimal impact on the electron beam dynamics and optics parameters.

Some relevant parameters for the Z and $t\bar{t}$ lattice options are reported in Table I.

The arcs, LSS, and FF optics matching the baseline layout are detailed in the following sections.

The optics presented in this document include: (i) arcs with a radius identical to baseline [2]; (ii) FF section length set to match the overall ring circumference: 90.66 km; (iii) 30 hybrid focusing defocusing (HFD) arc cells (see Fig. 2) in each octant; (iv) four 2032 m long straight sections (see Fig. 3); and (v) four final focus (FF) systems (see Fig. 4).

Specialized LSS optics for injection, collimation, beams crossing, and rf are presently not included. rf cavities are included for 6D tracking with SR and located in the LSS. Geometric constraints for the integration of the cryomodules or for swap from 400 to 800 MHz cavities as foreseen presently when going from Z to $t\bar{t}$ energy are not taken into account at this stage.

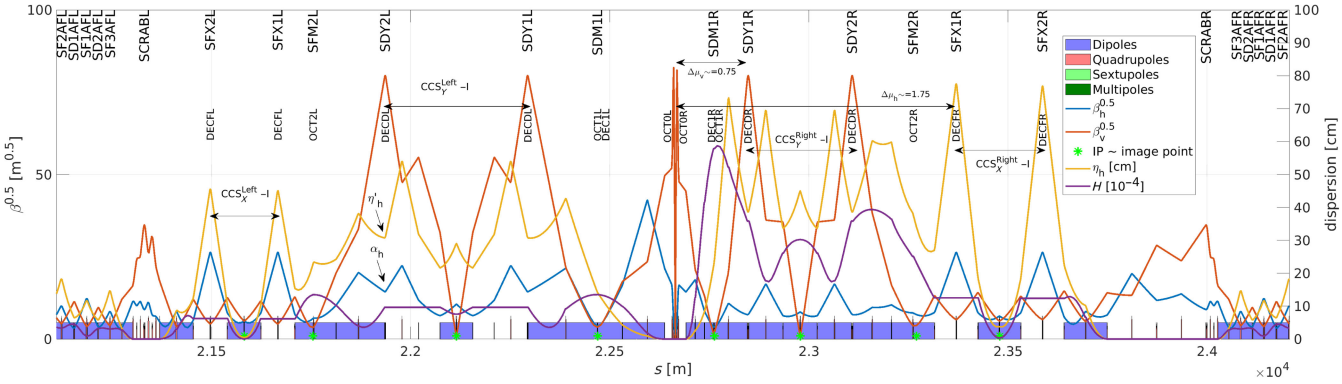

FIG. 4. One of the four final focus systems. The interaction point is located in the center of the displayed region. Sextupole names are reported in correspondence of their location. Crab sextupoles are named SCRAB. Green stars on the horizontal axis mark IP image point locations described in Sec. V.

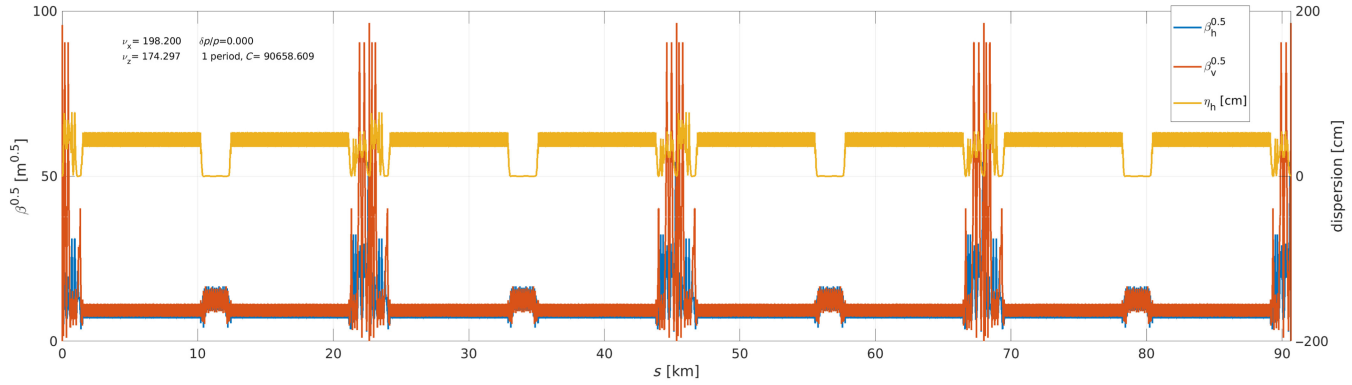

FIG. 5. LCC (version 92) lattice at Z including eight arcs, four long straight sections, and four final focus systems.

Figure 5 shows the whole lattice optics considered in the present work.

III. ARC LATTICE

A. Scaling of an FODO cell

High-luminosity colliders based on large Piwinski angle and crab waist (CW) [12,13] require very small equilibrium horizontal emittance ϵ_h and $\beta^*_{h,v}$. The small emittance leads to the need to increase the number of basic FODO cells in the arcs as much as possible.

In general, multiplying the number of cells (N_{cells}) of an FODO lattice by a factor n while keeping the circumference fixed (scaling all the elements proportionally) and keeping the basic cell phase advance constant results in (i) emittance decreases by n^3. (ii) Quadrupoles strength and number increase by a factor of n. (iii) Sextupole strengths increase by n^3 and number of sextupoles by a factor of n. (iv) Following the scaling rules in [5], momentum acceptance (MA) decreases by a factor of n, and dynamic aperture (DA) decreases by a factor $> n^3$.

The cost and power consumption of quadrupoles scale thus with N^2_{cells}. These scaling laws are confirmed by simulations in Fig. 6, where the circumference, tunes, and chromaticity are kept constant.

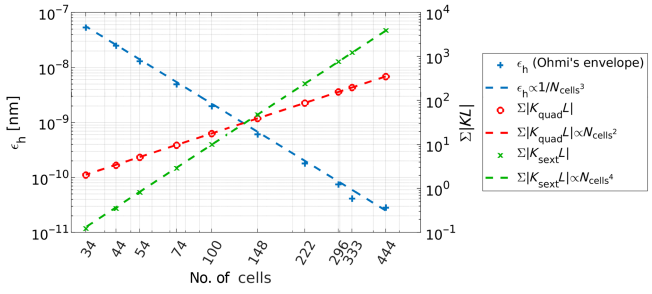

FIG. 6. Scaling of emittance, total quadrupole, and sextupole strength versus number of cells for an FODO lattice. Synchrotron radiation and tapering are included for horizontal emittance computations.

To limit the number of cells, the intrinsic arc cell emittance should be as small as possible. At the same time, the emittance increase due to insertions (e.g., FF) should also be minimized.

Anharmonicity and achromaticity become more severe with more cells. Figure 1 supports this statement by comparing FODO lattices with the increasing number of cells in the same total length.

B. HFD optics layout and matching criteria

The basic HFD cell (see Fig. 2) consists of ten dipoles (all of the same length), ten quadrupoles, and eight sextupoles [first QD1A and central QF6A quadrupoles do not need a sextupole]. The HFD cell is left-right symmetric. Quadrupole are grouped in two families ($QF*$ and $QD*$); sextupoles are grouped in four families as shown in Fig. 2.

The strengths of the quadrupole's and sextupole's families in one HFD cell are determined imposing optimal values for the following parameters: (i) K_{QF*}: horizontal natural emittance, selecting the corresponding μ_h; (ii) K_{SF1A} and K_{SF2A}: horizontal chromaticity $\xi_h \simeq 0$ and first-order variation of horizontal tune with horizontal amplitude $\frac{\partial Q_h}{\partial x} \simeq 0$; (iii) K_{QD*}: first-order variation of vertical tune with vertical amplitude $\frac{\partial Q_v}{\partial y} \simeq 0$ selecting the optimal μ_v (several μ_v fulfill this condition, lower values with respect to μ_h are preferred, see Sec. III C); and (iv) K_{SD1A} and K_{SD1A}: vertical chromaticity $\xi_v \simeq 0$ and first-order cross-term amplitude detuning $\frac{\partial Q_h}{\partial y} \simeq 0$, $\frac{\partial Q_v}{\partial x} \simeq 0$.

By adding additional quadrupole families (following the naming scheme in Fig. 2), further reduction of nonlinearities is possible.

The lattice characteristics are highly orthogonal with respect to the matching constraints.

These matching conditions generate a lattice with very small tune footprints (see Fig. 7).

The layout of the HFD arc visible in Fig. 2 is a standard FODO sequence with two missing sextupoles (at QD1A and QF6A) for every ten quadrupoles. BPMs are placed at each sextupole location (between sextupole and quadrupole).

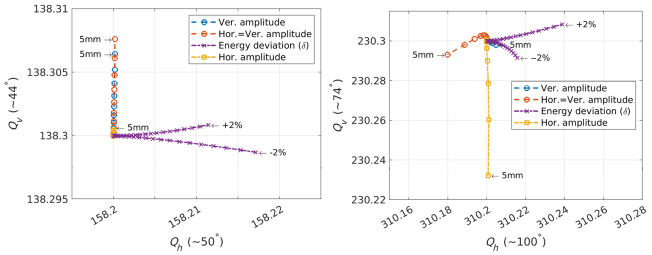

FIG. 7. Tune footprint of 224 unit cells for Z energy (left) and $t\bar{t}$ (right) for increasing horizontal amplitude, vertical amplitude, and energy deviation. The amplitudes are marked for each dimension considered.

C. Choice of the phase advance

The optimized HFD FODO average phase advance between consecutive quadrupoles ($QF*$ or $QD*$) for $t\bar{t}$ operation is about $(\mu_h, \mu_v) = (100, 74)$ deg. Weaker lattices utilize all the arc magnet complement at weaker settings (the same magnet layout is used for all energies). A weaker lattice with a phase advance of about $(\mu_h, \mu_v) = (50, 44)$ deg is achromatic and anharmonic as well; it is considered to be used for Z and W [1] operations and in general for any mode that requires a large momentum compaction. Both lattices have an MA in excess of $\pm 3\%$ and extremely large DA, as will be detailed later in Sec. III D.

The vertical phase advance μ_v has been chosen as the best compromise between chromaticities, detunings, and sensitivity to transverse collective effects (by limiting peak and average β functions). In Fig. 8, the HFD cell vertical phase advance μ_v is varied keeping constant the horizontal phase advance μ_h. In general, a vertical phase advance $\mu_v \simeq 0.8\mu_h$ results in lower chromaticity and relaxed requirements on magnets strengths, in particular sextupoles, while peak vertical beta functions (β_v) remain almost unchanged. Further lowering μ_v eventually leads to increased sensitivity to collective effects due to a larger average β_v.

Remarkably, peak $\beta_{h,v}$ are very similar for HFD phase advance choices $(\mu_h, \mu_v) = (100, 74)$ deg ($t\bar{t}$) and $(\mu_h, \mu_v) = (50, 44)$ deg (Z).

Figure 9 compares the optics function of a short FODO (90, 90) deg ($L = 52.4$ m) and the HFD (100, 74) deg.

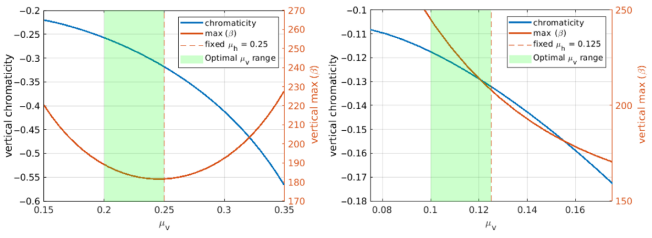

FIG. 8. Vertical chromaticity ($\partial Q_v/\partial\delta$) and maximum β_v in the HFD cell for varying vertical phase advance μ_v (2π units). On the left figure $\mu_h = 0.25$, while on the right figure $\mu_h = 0.125$.

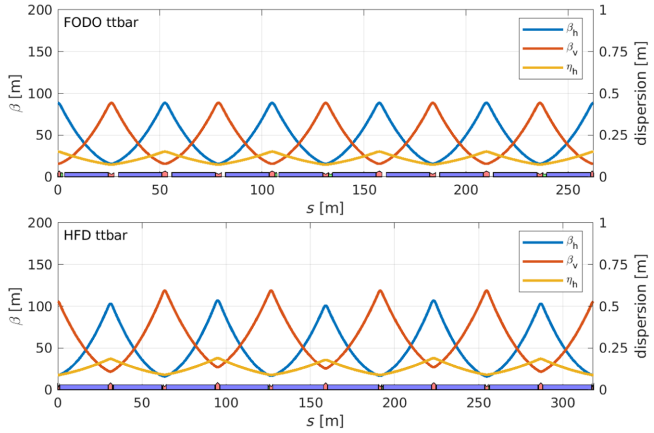

FIG. 9. Comparison of arc optics for $t\bar{t}$: an FODO (90, 90) deg short cell (top) and an HFD (100, 74) deg cell (bottom). Lattice sequences are periodic over ten dipoles.

Given the larger μ_h HFD needs fewer and longer cells to produce the same horizontal emittance. Figure 10 compares the optics function of HFD (50, 44) deg and FODO (90, 90) deg with about twice the cell length ($L = 106.8$ m). The GHC optics approach for the Z energy is to preserve the (90, 90) deg phase advance but double the length of the FODO lattice period (by switching off every other quadrupole). HFD optics, on the other hand, simply change the phase advance of the cell.

D. HFD dynamic aperture

A standard FODO lattice with a sextupole for every quadrupole is very achromatic but not anharmonic. The FODO with phase advance (90, 90) deg (adopted by the GHC optics) with noninterleaved sextupoles pairs placed at $-\mathcal{I}$ locations is less achromatic but more anharmonic. This is visible in Fig. 11.

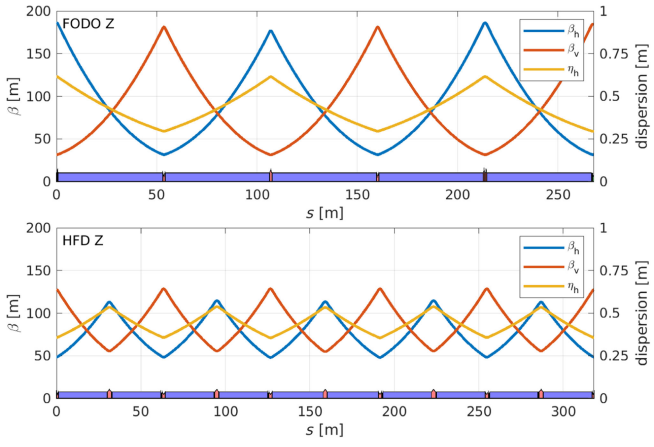

FIG. 10. Comparison of arc optics for Z: an FODO (90, 90) deg long cell (top) and an HFD (50, 44) deg cell (bottom). Lattice sequences are periodic over ten dipoles.

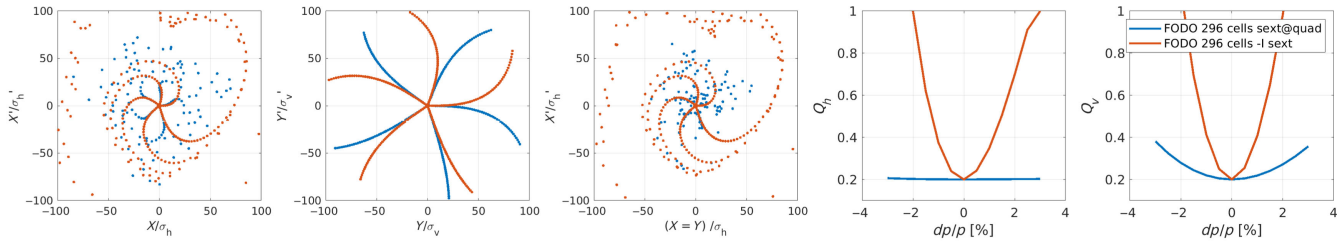

FIG. 11. Coordinates at each of five turns turns tracking particles starting on the horizontal axis (first plot on the left), vertical axis (second plot from the left), and for particles with identical horizontal and vertical coordinates (third plot from the left). The fourth and fifth plots show horizontal and vertical detuning with momentum. The curves refer to two FODO (90, 90) deg arc lattices with sextupoles at $-\mathcal{I}$ locations or at all quadrupoles. The lattice used is composed of eight arc cells, without LSS.

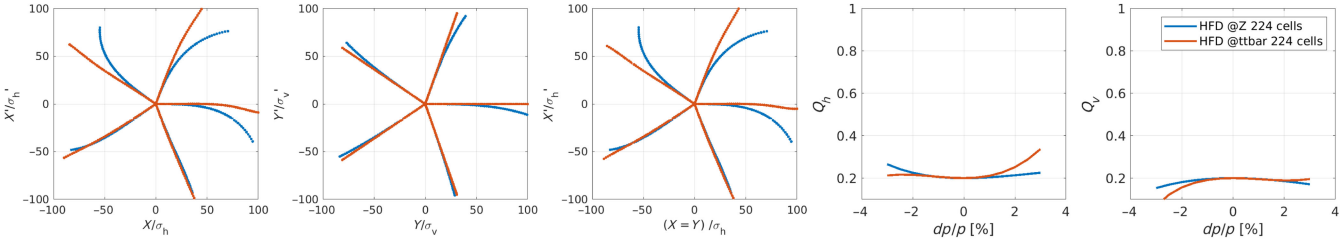

FIG. 12. Coordinates at each of five turns turns tracking particles starting on the horizontal axis (first plot on the left), vertical axis (second plot from the left), and for particles with identical horizontal and vertical coordinates (third plot from the left). The fourth and fifth plots show horizontal and vertical detuning with momentum. The curves refer to two arc lattice options: HFD with low phase advance (Z) and large phase advance ($t\bar{t}$). The lattice used is composed of eight ARC cells and eight LSS. Compared to Fig. 1 (same scales), HFD optics are the most anharmonic and achromatic options.

The ultimate source of high-order chromaticity for the GHC optics is uncorrected chromaticity and second-order dispersion driven by the quadrupoles with no nearby sextupoles.

For the HFD arc optics, both anharmonicity and achromaticity can be achieved simultaneously, as visible in Fig. 12. Other approaches may be followed. For example, the CEPC (Circular Electron Positron Collider) collider strategy is to cancel the second-order chromaticity with sextupole families encompassing eight cells [14].

For the HFD optics, it is in fact possible to remove the second-order chromaticity while still maintaining the (geometric) properties of the noninterleaved sextupoles scheme. The linear detuning can be canceled by adjusting the phase between the sextupole pairs to nonexact $-\mathcal{I}$ transformations. This technique can be applied for any given cell phase advance. This technique is effective when the fractional horizontal cell phase advance is close to 90 deg because sextupole tends to be close to $-\mathcal{I}$ transformation. However, for lower phase advance, the chromaticity decreases very fast; thus the intrinsic nonlinearities from the sextupoles become very weak. In fact, the lower phase advance lattice for Z energy has much larger DA and MA with respect to tt bar. Natural chromaticity is shown for FODO and HFD lattice options in Table II, showing how the HFD optics provide lower values.

The HFD lattice includes four sextupole families. These additional degrees of freedom allow for the determination of anharmonic and achromatic solutions for a continuous range of μ_h between 30 and 110 deg. HFD arc lattice with $(\mu_h, \mu_v) = (50, 44)$ deg and $(\mu_h, \mu_v) = (100, 74)$ deg produces machine parameters that closely match those of the FCC-ee CDR [1].

The transverse DA and MA of a ring composed of HFD arc cells only (without FF and LSS) are extremely large for both Z and $t\bar{t}$ optics as visible in Fig. 13. For reference in the same figure also the DA of an FODO (90, 90) deg lattice is shown. The advantages of a detuning free lattice are evident.

HFD optics provide simultaneously very large transverse and momentum acceptance.

E. Magnet requirements

The HFD cell dipoles are about 29.6 m long. QD and QF quadrupoles are 1.8 and 2.4 m long, respectively.

TABLE II. Natural chromaticity for HFD and FODO arc optics at two FCC-ee operating energies.

Optics	Energy	ξ_h	ξ_v
HFD	Z	−159.60	−156.62
FODO	Z	−236.13	−235.81
HFD	$t\bar{t}$	−380.81	−313.71
FODO	$t\bar{t}$	−471.38	−471.38

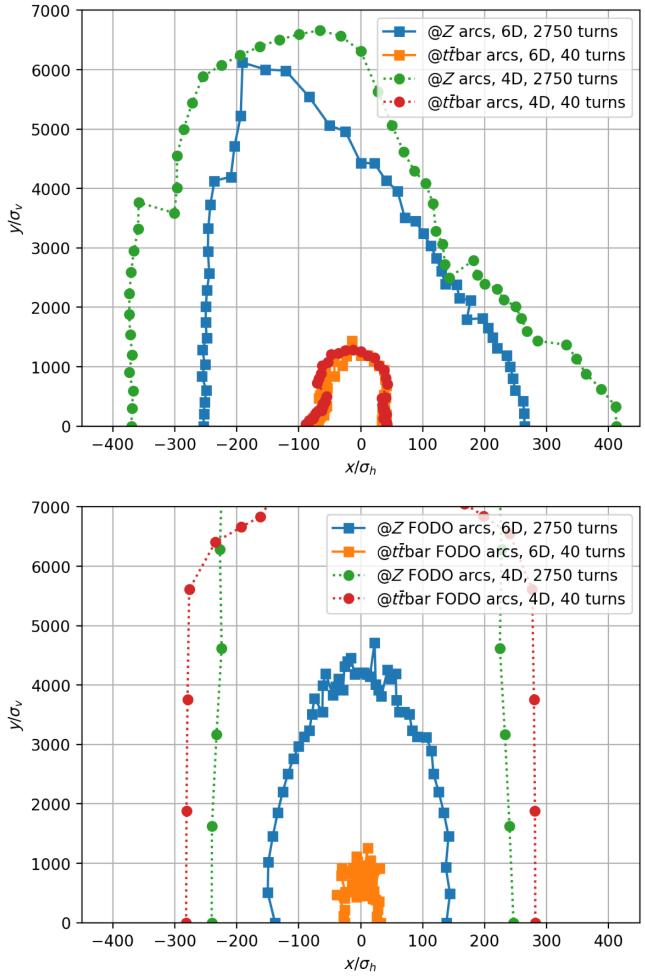

FIG. 13. Transverse dynamic aperture for FCC LCC arcs (top) and FODO (90, 90) deg arcs (bottom) at Z and $t\bar{t}$ energy computed at the center of QD1A. The 6D tracking for one damping time includes quantum diffusion and synchrotron radiation.

A total of 2240 quadrupoles per ring are needed for the arcs. SD and SF sextupoles are 50 and 35 cm long, respectively, making use of the sextupole design [1,15] already available for the baseline optics. Dipoles have all the same length so the e^+/e^- arcs can be longitudinally shifted to align opposite polarity quadrupoles for the two rings. Twin quadrupoles [1] and an additional short QF (60 cm long) can be used to replace the QF/QDs of the two arcs. If high temperature superconducting [16] magnets are used, quadrupoles do not need to be paired and the sextupole coils can be wrapped around the quadrupole ones, thus improving the dipoles filling ratio and reducing the horizontal natural equilibrium emittance. The sextupoles design is consistent with the FCC baseline one. Trim coils are foreseen on the sextupoles for orbit (horizontal and vertical correctors) and optics correction (normal and skew quadrupole). No additional correctors are needed.

IV. LONG STRAIGHT SECTION MATCHING

The insertion of the straight sections (see Fig. 3) is performed by requiring the *Transparency Conditions* described in [5]. This allows to insert any straight section (SS) in a ring magnetic lattice, without any significant degradation of its characteristics (DA/MA, detuning, etc.), despite the symmetry breaking. Moreover, this approach does not require the introduction of additional sextupole families. The TCs can be applied for any given SS, provided that enough quadrupoles are available to match the conditions on each side of the long straight section.

A. Transparency conditions

For a left-right symmetric insertion section, the TCs are reported here for completeness (all these conditions are achieved by linear optics matching): (i) conditions to ensure that the arc optical functions periodicity is kept for the on-energy electrons: (a) $\alpha_h = \alpha_v = \eta' = 0$ (optics matching condition) at the center of the straight section; (ii) conditions to ensure the nonlinear transverse dynamic transparency (with N and M integer numbers): (a) $\Delta\mu_h = 0 + N$, (b) $\Delta\mu_v = 0 + M/2$, where $\Delta\mu_{h,v}$ are the additional phase advances (in units of 2π) generated by the insertion; (iii) conditions to ensure that the optical functions periodicity is kept for the off-energy electrons as well (at first order) (a) $\frac{\partial W_h}{\partial s} = \frac{\partial W_v}{\partial s} = \frac{\partial \eta'}{\partial s} = 0$, with $W_{h,v}$ the Montague functions defined in [8] evaluated at the center of the straight section.

In general, high-order contributions are reduced if (i) for a superperiodic lattice (arcs+SSs), the phase advance between arcs is far from 0 and 0.5. The overall integer part of the tunes should not be a multiple of the superperiodicity. (ii) The overall chromaticity of the straight section is minimized as much as possible.

Observing Fig. 3, only the linear optics between the last and first sextupoles of the adjacent arcs are modified. The matching quadrupoles are between QFS0A and QFS5A.

B. Dispersion suppressor and long straight

For FCC, the cells on either side of the long straight sections are dispersion suppressors (DS) cells (see Fig. 3).

In order to match first- and second-order dispersion, four dipoles in the arcs on each side of the straight section have optimized tapered lengths. Compared to a simple missing dipole dispersion suppressor scheme, this solution allows to easily match second-order dispersion.

At the end of the DS, harmonic sextupoles are inserted (for example, SF3ASR in Fig. 3) in order to further improve the dynamic aperture and possibly optimize the phase space shape in the straight sections.

Matching the sections following the TCs guarantees the periodicity of the chromatic functions. They remain periodic with sextupoles off and on as shown in Fig. 14. No additional sextupole families are needed to restore chromatic properties up to the third order.

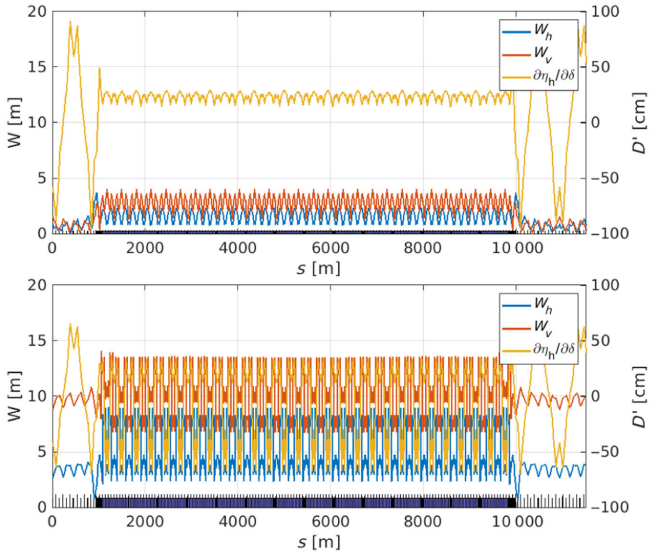

FIG. 14. *W* functions and dispersion derivative with energy for one octant of the LCC FCC lattice. Both off-energy optics functions are periodic with sextupoles OFF (top) and ON (bottom) for a lattice composed of arcs and LSS.

A lattice composed of arc+LSS has small second and higher order chromaticity terms in both planes that do not limit the MA at least up to ±3% (see Fig. 12).

C. Use of HFD and LSS to design other lattices

HFD produces highly anharmonic and achromatic arc cells. HFD matching criteria work well to build quasilinear lattices for a large range of cell phase advances.

Overall, MA above ±5% can be achieved for a ring composed of up to 300 cells. HFD could be used for low-emittance rings, damping rings, and synchrotron light sources as well. TCs are a simple and analytical method to insert special sections in the arc preserving the ring DA and MA of the fully periodic structure.

V. FINAL FOCUS

The final focus has been dimensioned to meet the parameters and requirements (layout, synchrotron radiation, geometrical constraints, etc.) of the FCC-ee baseline design [1].

LCC requirements are fulfilled in the Final Focus sections by correcting the low-β IP chromaticity within the FF in both planes and nearly entirely. In order to minimize the crab sextupoles [17] impact on the MA, they are placed in a nearly achromatic region: the FF outer ends (see Fig. 4, SCARBL and SCRABR magnets). This solution has been developed for the SuperB [6] and has been adopted by CEPC [14] as well.

Half FF (incoming or outgoing) is basically a telescope that starts after the arcs dispersion suppressor and ends at the IP. The FF is built to be as much as possible a high-order achromat in both planes. In this section, the methods used to optimize the FF will be described as well as the definitions of the related tuning knobs and their effect on overall performances. This methodology can be applied very generally to any low β insertion. By construction, the whole FF is an identity transformation and can be readily inserted in the ring according to the TCs criteria. Each knob in fact targets a specific detuning with momentum term. Special locations with an integer phase advance with respect to the IP called *IP-phase* or *IP image points* (see Fig. 4) are available in the optics and are used to place dedicated magnets. Magnets in these locations are almost as effective as magnets placed directly in the proximity of the IP or the final doublet and thus may be used to create very powerful tuning knobs. The main knobs used to tune the FF are (i) sextupoles SD_y and SF_x to correct almost completely the final doublet (FD) chromaticity in both planes ($\frac{\partial Q_{h,v}}{\partial\delta}$). (ii) SD_y and SF_x sextupoles phase advance, with respect to the IP, to set second-order chromaticity to zero ($\frac{\partial^2 Q_{h,v}}{\partial^2\delta}$). The sextupoles should be in phase with the main chromaticity source (the FD). (iii) IP-phase sextupoles SDM and to correct third-order chromaticity ($\frac{\partial^3 Q_{h,v}}{\partial^3\delta}$). (iv) IP-phase octupoles for fourth-order chromaticity. (v) IP-phase decapoles for fifth-order chromaticity. (vi) Decapoles pairs in CCS_X and CCS_Y to correct off-energy dependent x, y, and x-y detuning with amplitude. (vii) Phase advance between $-\mathcal{I}$ sextupole pairs in horizontal and vertical chromaticity correction sections (CCS_X and CCS_Y) reduces the $\frac{\partial Q_h}{\partial x}$, $\frac{\partial Q_v}{\partial y}$, and $\frac{\partial Q_{h,v}}{\partial(x=y)}$ amplitude detuning coefficients due to the long sextupole aberration [18].

The dipoles distribution in the lattice optics has also to be optimized to minimize aberrations related to high-order dispersion.

A. Final focus chromatic correction

In order to evaluate the performance of the FF optics design, the observables are variations of β and α at the IP versus energy deviation and detuning with momentum. Figures 15 and 16 show these curves for various FF configurations to better visualize the effect of each element added to the FF design. From Fig. 15, the MA at the IP can be also estimated. In particular, the FF MA without chromatic compensation (all sextupoles OFF) is infinitesimal.

First-order chromatic correction is obtained by tuning the main SD_y and SF_x pairs (see Fig. 4) in order to zero the derivatives of α_h and α_v with respect to energy (see Fig. 16). For second-order chromatic correction, the phase advance between the sextupole pairs SF_x and SD_y (see Fig. 4) with respect to the IP is optimized (see Fig. 15). The optimal value is close but not equal to $(N + 1/2)\pi$ rad, to take into account the other small chromatic contributions

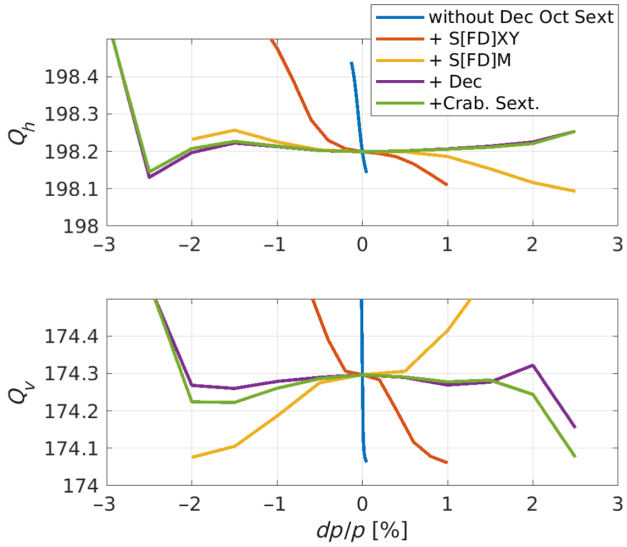

FIG. 15. Tunes versus momentum introducing one by one the nonlinear multipoles in the final focus optics. Results are obtained by 6D particle tracking without synchrotron radiation.

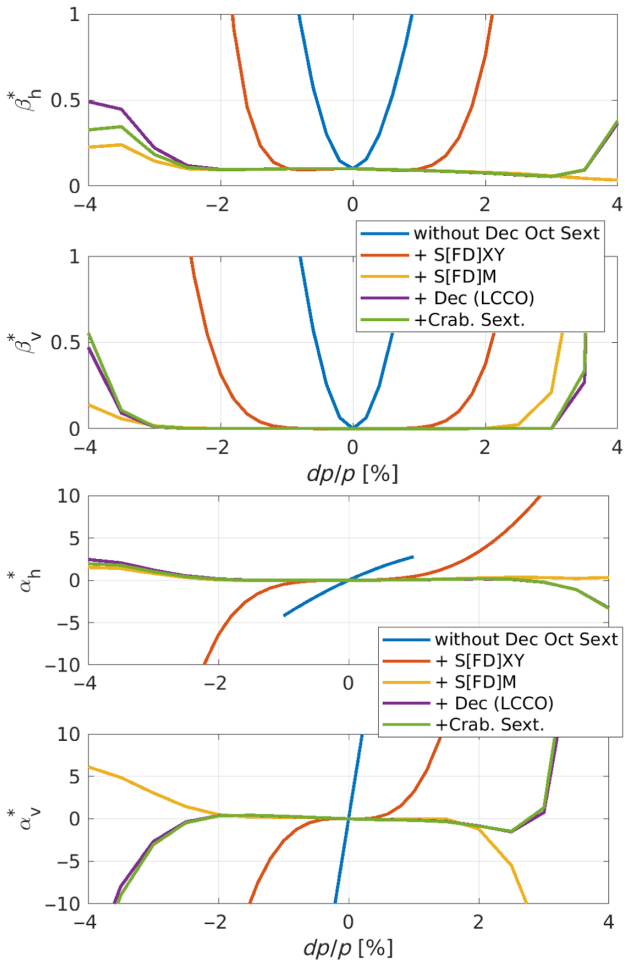

FIG. 16. $\beta*$ at IP (top) and $\alpha*$ at IP as a function of the energy deviation considering only the FF optics turning on progressively the multipoles for nonlinear corrections.

(at different phases) from the other quadrupoles in the FF. The optimal phases are set with simple linear optics matching. The quadrupoles available in the lattice allow the change of these phases while maintaining all the other parameters unchanged ($\beta_{h,v}$, $\alpha_{h,v}$, $\eta_{h,v}$, $\eta'_{h,v}$, and $\Delta\mu_{h,v}$ at relevant locations). Higher order chromatic terms remain, in particular, the third order is visible in Figs. 15 and 16.

The chromatic behavior for an off-energy beam is heavily affected by third-order chromaticity. Optics (β and α) at the crab sextupoles (CS) are still strongly varying off-energy (still the variation is smaller than if no action was taken): $\beta_h^{\mathrm{CS}} \sim 100$, $\beta_v^{\mathrm{CS}} \sim 400$ (see Fig. 17).

Sextupoles are less effective in correcting the chromaticity for off-energy electrons. The reason is that the β functions at the sextupoles for off-energy particles are lower (see Fig. 17), so they do not correct the chromaticity effectively anymore and also the relative phase with respect to the final doublet (FD) changes.

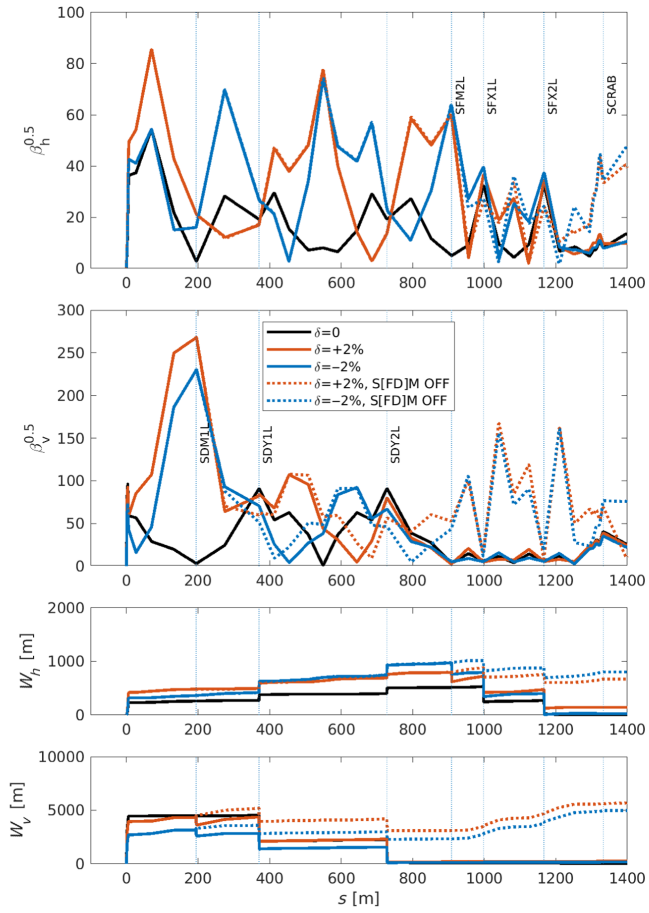

FIG. 17. FF β functions, dispersion, W functions, and second-order dispersion at $\delta p/p = \pm 0.2\%$ with and without IP-phase sextupoles SFM and SDM, starting from the IP. Tracking is performed assuming the FF as a transfer line and using the on-energy IP $\beta^*_{h,v}$ as input values.

B. Final focus high-order chromatic corrections

The two additional weak sextupoles are added in the IP image points (SFM and SDM, IP-phase sextupoles) outside the $-\mathcal{I}$ pairs. Since they are at low β locations, they do not harm the FF anharmonicity. Off-energy vertical β functions at the SDM location become very large. Similarly off-energy horizontal β functions at the SFM location. Thus, the SFM and SDM sextupoles are very effective in restoring the nominal $\beta_{h,v}$ of the main sextupoles for all energies. The $\beta_{h,v}$ at the crab sextupoles (SCRABR) become close to nominal for all energies as well (see Fig. 17). Using SFM and SDM sextupoles, the chromaticities are well corrected for on- and off-energy beam as well. The contribution of the IP-phase sextupoles for the off-energy beam is evident (see Figs. 15, 16, 17). The IP-phase SDM and SFM sextupoles make the FF a third-order achromat. To match the arcs W functions, a linear chromaticity different from zero has been set. The remaining terms above the third order are visible (on a large scale) in Fig. 15 and their effect on the variation of optics at the IP versus energy in Fig. 16. Following the same principle, an octupole at the same location of the SDM can cancel the fourth-order chromaticity and a decapole can cancel the fifth-order chromaticity.

C. Final focus geometric aberrations

The long sextupole aberration has a large contribution on the DA. The corresponding amplitude detuning coefficients can be reduced by adjusting the $-\mathcal{I}$ transformation between the $\mathrm{CCS}_{Y/X}$ SD_y s and SF_xs pairs to be slightly different from exactly $-\mathcal{I}$. Optimal phase advances difference from π is of the order of 10^{-3} rad. In fact, the optimal values are determined by zeroing the overall detuning contribution introduced by the final focus (fringe fields, octupoles, SDM, and SFM).

D. Final focus geometry

The FF geometry (see Fig. 18) is adjusted in order to recover entirely the IP crossing angle, thus having parallel beams entering the arcs, such that modifications to arc's dipoles are not necessary. At the end of the FF, the e^- and e^+ beams are parallel and separated by 40 cm. This is achieved using (following the trajectory of the beam): (i) short $\mathrm{CCS}_X^{\mathrm{Left}}$ section with "strong bends"; (ii) long $\mathrm{CCS}_Y^{\mathrm{Left}}$ section with "weak bend"; (iii) short $\mathrm{CCS}_Y^{\mathrm{Right}}$ section with strong bends; and (iv) long $\mathrm{CCS}_X^{\mathrm{Right}}$ section with weak bend.

1. Left FF

Figure 4 shows the FF optics. The last four dipoles before the IP have a critical energy, $E_c \sim 130$ keV, consistent with the FCC-ee $t\bar{t}$ synchrotron radiation requirement. $\mathrm{CCS}_Y^{\mathrm{Left}}$ optics produces a large dispersion at the sextupoles for a given bend angle in the $-\mathcal{I}$ regions (see Fig. 4).

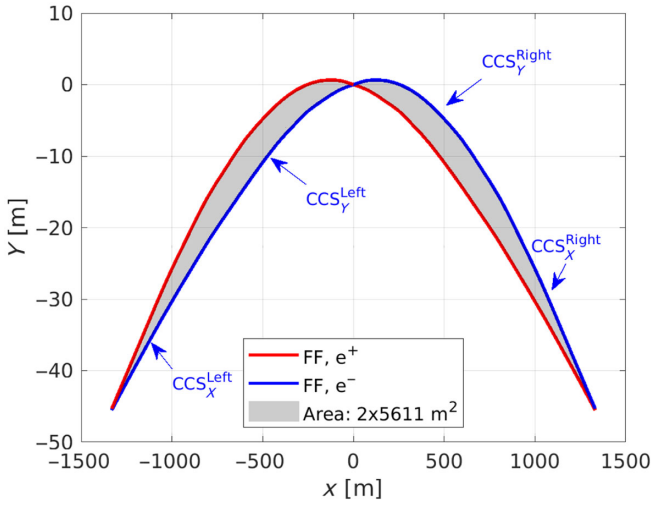

FIG. 18. Footprint in Cartesian floor coordinates of the low-β insertion.

Lengths and bending angles of the $\mathrm{CCS}_Y^{\mathrm{Left}}$, $\mathrm{CCS}_X^{\mathrm{Left}}$, $\mathrm{CCS}_Y^{\mathrm{Right}}$, and $\mathrm{CCS}_X^{\mathrm{Right}}$ dipoles are optimized to have maximum dispersion on $\mathrm{CCS}_Y^{\mathrm{Left}}$ and minimum overall emittance growth and SR. The CCS_Y sextupoles are 0.6 m long and are very weak with $K_{\mathrm{sext}} \sim 0.7$ m^{-2} at $t\bar{t}$ and $K_{\mathrm{sext}} \sim 0.9$ m^{-2} at Z energy. In fact, the arc sextupoles design (magnetic and mechanical) can be used in the FF as well.

2. Right FF

All the dipoles in the $\mathrm{CCS}_Y^{\mathrm{Right}}$ have the same field, as this is the best configuration to recover the beams separation in the most effective way space wise with minimal synchrotron radiation. Similarly, $\mathrm{CCS}_Y^{\mathrm{Right}}$ optics have been optimized to obtain the largest dispersion, given this dipole configuration. The nonlinear optimization detailed in the previous section is performed independently for the two sides of the FF. A very long dispersion free straight section, ~400 m is present in the dispersion suppressor of the right side of the FF. Two drifts, each about 100 m long, are also present in the $\mathrm{CCS}_X^{\mathrm{Right}}$ $-\mathcal{I}$ transformation region. These straight sections could be used to accommodate diagnostics such as polarimeters and emittance monitors among others.

Fine-tuning of the linear optics in the FF left and right allows to have W functions and second-order dispersion derivative at the end of the FF matching those of the arcs.

For example, the dispersion derivative $(\partial\eta_x/\partial s)$ in the center of the CCS_X is used to equal left and right FF $\frac{\partial^2\eta_x}{\partial s\partial\delta}$, thus avoiding the beating of the second-order dispersion $(\frac{\partial\eta_x}{\partial\delta})$ in the ring. α_y in the center of CCS_X is used to equal left and right $\frac{\partial\alpha_y}{\partial\delta}$, thus avoiding the beating of the W functions in the ring.

This tuning is very effective when done numerically as will be described later in Sec. VI.

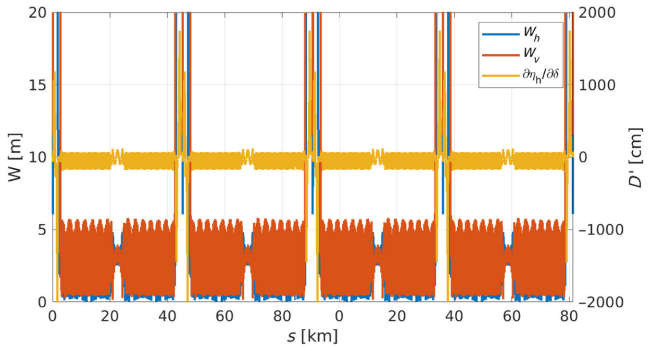

FIG. 19. Full-ring chromatic properties: W functions and dispersion derivative with energy. In the IP region, the W functions reach ∼5000 units.

The tuning of the dispersion derivative in the center of the CCS is also applied to α_y in the $\mathrm{CCS}_X^{\mathrm{Right}}$ and $\mathrm{CCS}_X^{\mathrm{Left}}$ (that is different from zero). This makes the β_v functions asymmetric at the CCS sextupoles (SD_y and SF_x) but restores symmetry in the FF nonlinear optics (W functions and dispersion derivative) at the left and right side of the IP.

E. Full-ring chromatic properties

W functions in the arcs are periodic, and their maximum amplitude is about 6 units in both planes (see Fig. 19). As mentioned before, arc sextupoles are not needed to correct the FF chromaticity. The FF sextupole pairs are set to match the arc W functions at the FF exit. Given this "quasi-Full Achromat" condition, there is no need to change the arcs and FF sextupoles (and crab sextupoles) settings when the β squeeze is done with the β-matching quadrupoles. Looking at Fig. 17, any beam entering the FF, independent of the energy (achromatic) and amplitude (anharmonic), will be focused at the IP. Moreover the β functions at the exit of the FF are also independent from the energy up to $\sim \pm 2\%$.

Since the LCC FF optics are very achromatic, there is no luminosity loss for off-energy particles. This feature will be extremely effective to reach top performances when changing the β^* at each IP. Luminosity leveling by tuning individually the four IPs β^* is straightforward.

F. Cancellation of the energy dependent Y and X-Y detuning with decapoles

The $-\mathcal{I}$ condition between the CCS sextupole pairs is broken for off-energy particles. Given the large β functions at the sextupoles, this generates very strong detuning coefficients (in ascending order of relevance):

$$\frac{\partial^2 Q_v}{\partial x \partial \delta}, \quad \frac{\partial^2 Q_v}{\partial y \partial \delta}, \quad \frac{\partial^2 Q_h}{\partial x \partial \delta}, \quad \frac{\partial^2 Q_h}{\partial y \partial \delta}.$$

Decapole pairs adjacent to the sextupoles are very powerful enough to cancel those aberrations without introducing geometric aberrations because of the cancellation due to the $-\mathcal{I}$ transformation (as for sextupoles). FF left and right decapoles pairs (DECF and DECD in Fig. 4) are tuned to achieve global cancellation instead of targeting the properties of each side of the FF individually. In fact, only two decapole pairs are available in each side of the FF, whereas three aberrations have to be canceled. The decapole knobs are: (i) $\mathrm{CCS}_y^{\mathrm{Left}}$ decapoles are negative and cancel xy-detuning at $\delta \neq 0$. (ii) $\mathrm{CCS}_y^{\mathrm{Right}}$ decapoles are positive and cancel y-detuning at $\delta \neq 0$. (iii) $\mathrm{CCS}_x^{\mathrm{Left}}$ and $\mathrm{CCS}_x^{\mathrm{Right}}$ decapoles are positive and cancel x-detuning at $\delta \neq 0$.

$\beta_{h,v}$ at $\mathrm{CCS}_y^{\mathrm{Left}}$ $\mathrm{CCS}_y^{\mathrm{Right}}$ are set to maximize the decapole effectiveness as listed in Table III.

TABLE III. Optics and decapole's strengths in the FF at $t\bar{t}$ energy.

Section	Name	β_h (m)	β_v (m)	η_h (m)	K_{dec} (m^{-4})
CCS_x^{Left}	DECFL	693	22	0.46	+90
CCS_y^{Left}	DECDL	207	6400	0.31	−900
CCS_y^{Right}	DECDR	55	6400	0.39	+1300
CCS_x^{Right}	DECFL	692	35	0.77	+60

Figure 20 shows the effect of the decapoles on the off-energy phase space.

Each decapole pair is very effective for a specific detuning, given the large difference in β functions.

High-order residual nonlinearities (mainly vertical) due to the CCS_Y decapoles are canceled altogether because of the opposite sign of the left/right decapoles. β_h at DECDL is much larger than at DECDR. So DECDL is effective to cancel the cross-term detuning ($\frac{\partial^2 Q_{v(h)}}{\partial x(y)\partial\delta}$), whereas DECDR is effective to cancel the vertical detuning ($\frac{\partial^2 Q_v}{\partial y \partial \delta}$). There are no side effects on the DA and on on-energy detuning coefficients. The third-order chromaticity is weakly affected. This results in a small change in the IP-phase sextupoles settings, making the horizontal IP-phase sextupoles (SFM) 10% weaker.

1. Dynamic aperture with and without SR

The effectiveness of the $-\mathcal{I}$ decapoles pairs (near to SD_y and SF_x sextupoles) to recover the on-energy transverse dynamic aperture in the presence of synchrotron radiation is evident from Fig. 21. The DA reduction in the presence of synchrotron radiation is dominated by the FD quadrupoles. By reducing the off-energy detuning coefficients with decapoles, the DA reduction due to synchrotron radiation is lowered. This is a novel approach to effectively address the degradation due to the quadrupoles (in particular the FD) synchrotron radiation. With synchrotron radiation, the beam loses energy quadratically with the action; however, with decapoles, it experiences greatly reduced detuning coefficients (see Fig. 20).

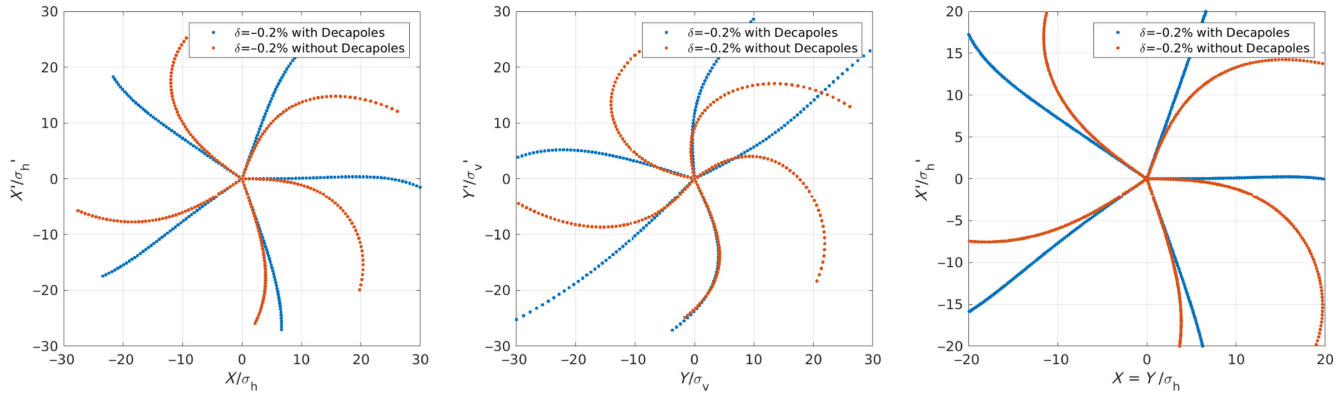

FIG. 20. Starfish plots for different decapoles settings at $\delta = -0.2\%$. Tracking is performed with synchrotron radiation and with crab sextupoles set to zero.

The decapole values can be determined analytically. The breaking of the $-\mathcal{I}$ between CCS sextupoles due to chromaticity generates an octupolar term proportional to

$$K_{\mathrm{oct}} \propto K_{\mathrm{sext}}^2 \delta.$$

Similarly, a decapole at the same sextupole location may be set to generate an octupolar term for off-energy particles proportional to

$$K_{\mathrm{oct}} = 4K_{\mathrm{dec}}\eta_h\delta.$$

The strength of the decapoles (K_{dec}) are chosen to cancel the octupole strengths (K_{oct}) introduced by the sextupoles.

G. Sensitivity of the FF sextupoles parameters on DA and MA

FF sextupoles strengths are driven by the chromaticity generated by the quadrupoles necessary to obtain low-β functions at the IP, which are defined by luminosity considerations. Larger β-functions at sextupoles do reduce the sextupole strength but have little effect on error sensitivity. Larger dispersion at sextupoles reduces their strength as well and consequently: (i) decreases as $\propto 1/\eta$ the waist shift (betatron mismatch) due to horizontal orbit error; (ii) decreases as $\propto 1/\eta$ the coupling due to vertical orbit error; (iii) decreases as $\propto 1/\eta^2$ (or more) the residual nonlinear geometric (and some chromatic) aberrations; and (iv) does not affect the dispersion mismatch due to orbit errors.

Larger dispersion is, in general, beneficial, provided that the second-order dispersion is properly compensated and the SR from stronger dipoles does not impact the IP area radiation handling and the emittance. LCC FF has much higher dispersion at the SDs with respect to the baseline

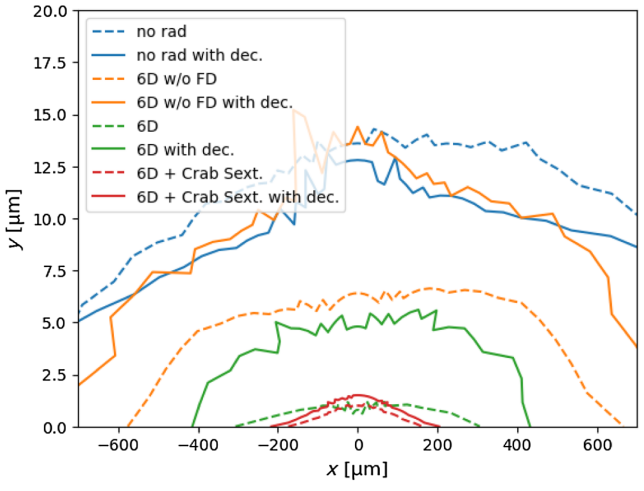

FIG. 21. Transverse dynamic aperture without and with decapoles in the FF in the presence of synchrotorn radiation: in none of the magnets, in all the magnets apart the final doublet (FD), and in all magnets. This last case is reported also with crab sextupoles turned on.

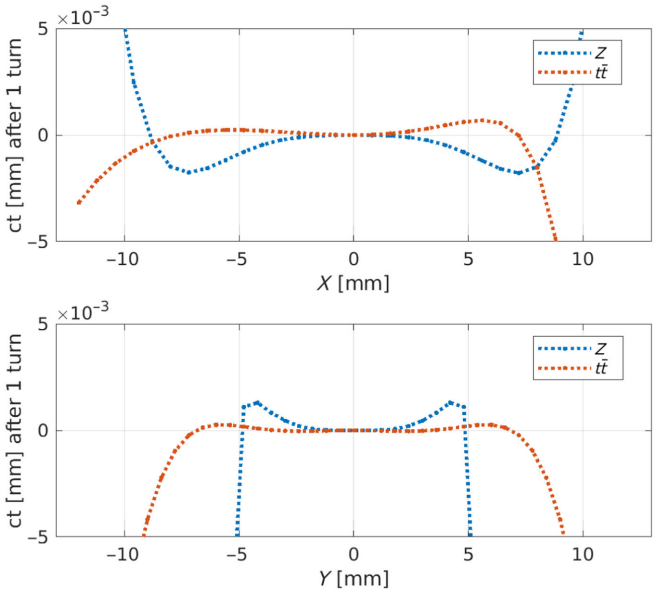

FIG. 22. Path lengthening versus amplitude for the LCC optics at Z and $t\bar{t}$ energies as observed at the center of the straight sections. High-order momentum compaction terms are negligible.

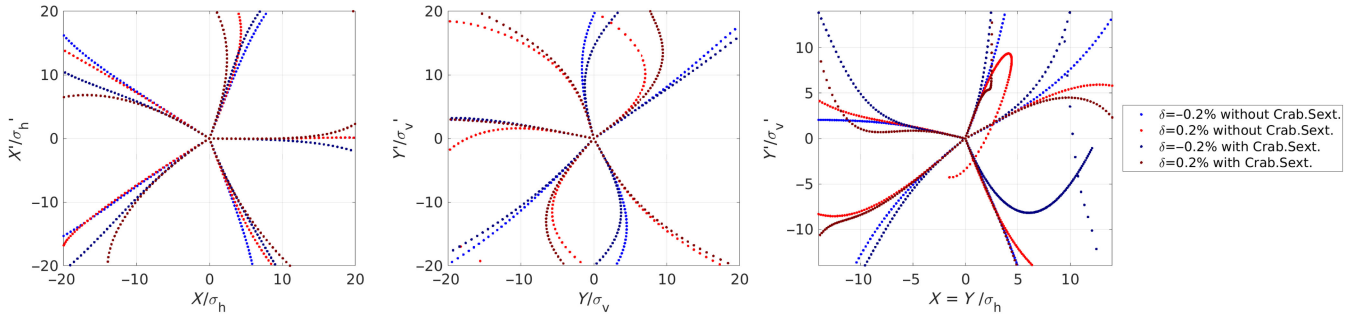

FIG. 23. Off-energy ($\delta = 0.2\%$) starfish plot with and without CS. A strong detuning with amplitude for off-energy particles with CS on is visible in the $X = Y$ phase space ($\frac{\partial^2 Q_{h,v}}{\partial\delta\partial(x=y)}$).

FCC optics. Henceforth, lower sensitivities to errors are expected (see Sec. VIII).

In addition, the large dispersion across the FF sextupole pairs reduce fourth and higher order path lengthening with amplitude (see Fig. 22). Overall, path lengthening has negligible effect on beam dynamics. With the LCC optics design, the on-energy dynamics are linear (see Fig. 12): resonances are virtually nonexistent. Those are extremely favorable beam conditions to minimize unwanted beam-beam effects [19], in particular lifetime in collision.

H. Optimization of optics with crab sextupoles

Preservation of the DA with CS set for optimal luminosity (later called CS *on* state) is critical. In order to minimize the impact of turning on the CS, the optics have been optimized as follows: (i) Reduce all nonlinearities between the CS. In particular, the nonlinearities due to the $-\mathcal{I}$ pair sextupoles and the ones from the IP-phase sextupoles. R_{12}/R_{34} between the $-\mathcal{I}$ pair sextupoles are optimized with CS on. This optimization is also valid for CS off. (ii) Reduce the strength of the IP-phase sextupoles by increasing η_h on the sextupoles. (iii) Optimized $\beta_{h,v}$ and $\alpha_{h,v}$ at the IP-phase sextupoles. (iv) Flattened $\beta_{h,v}$ versus δ at the CS. (v) Zeroed η_h versus δ at the CS.

The last two bullet points are equivalent to achieving a section that is a perfect achromat between the left and right CS (see also Fig. 17). On-energy nonlinearities due to the CS are relatively weak. However, CS do introduce a very strong $\frac{\partial^2 Q_{h,v}}{\partial\delta\partial(x=y)}$,with quadratic behavior with respect to the CS strength. This effect is visible in the off-energy *starfish* phase space plot of Fig. 23.

This aberration is partially compensated with the FF decapole complement. Further optimizations of the optics in order to make the decapoles more effective have to be foreseen.

I. Magnets requirements

There are no reverse bends in the FF, thus simplifying the SR handling for the distributed absorbers.

The stronger dipoles are in the $\mathrm{CCS}_y^{\mathrm{Right}}$ just downstream the IP, they are anyway about 10% weaker with respect to the arcs ones.

The "soft bend" upstream of the IP is about 230 m long with a SR critical energy $E_c \sim 130$ keV at $t\bar{t}$ energy.

Overall, the ratio of energy loss/bending angle $U_0/\theta|^{\mathrm{Z,FF}} = 5.44$ MeV/rad in the FF is very similar to the arc one $U_0/\theta|^{\mathrm{Z,arcs}} = 5.46$ MeV/rad. Henceforth, U_0 is very close to the minimum possible (that of an accelerator without FF insertions).

No superconducting magnets are required, except for the FD ones. FF quadrupoles are shorter and weaker compared to the arc's. The sextupole strengths of this lattice, compared to the baseline GHC design, are shown in Fig. 24. FF sextupoles have integrated K values similar to the ones required in the arcs. The sextupoles K_{sext} for the Z optics are about 5 times weaker with respect to $t\bar{t}$ optics.

Figure 25 shows the total number, integrated lengths, and integrated strengths (absolute values) for the magnets of the LCC optics and GHC optics. The overall requirements for number of magnets, total lengths of magnets, and integrated strengths are heavily reduced for LCC optics with respect to GHC optics. In particular, LCC lower

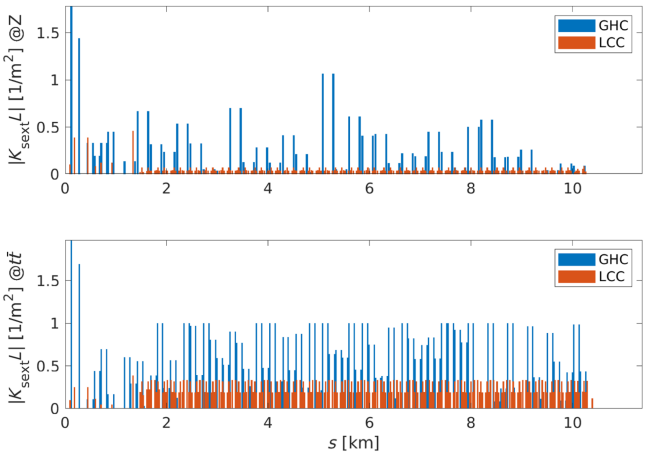

FIG. 24. Sextupole strengths for one octant of the GHC [2] and the LCC lattice optics.

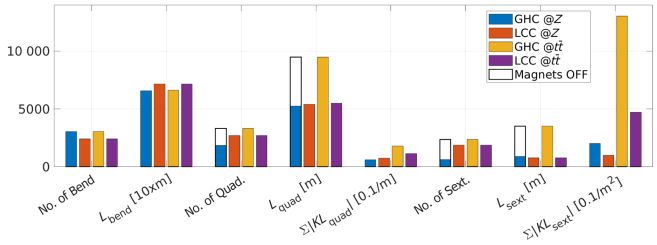

FIG. 25. Total number, integrate lengths, and integrated strengths (absolute values) of dipoles, quadrupoles, and sextupoles for LCC and GHC optics at Z and $t\bar{t}$. Black profiles indicate that those magnets are present but not active.

integrated sextupole strengths are a consequence of lower arc lattice chromaticity and local chromatic correction of the low-β insertions. The total power consumption required for sextupoles and quadrupoles is about 2–3 times lower.

VI. NONLINEAR OPTIMIZATION USING NUMERICAL ALGORITHMS

Starfish plots and detuning with momentum can be computed rapidly and therefore, in the case of large rings, such as the FCC, provide convenient observables to manually optimize the lattice nonlinear dynamics. However, injection efficiency and lifetime are more representative of the machine's performance and can be easily measured and optimized in the control room. It is, therefore, useful to optimize directly these two quantities in simulations to evaluate the tunability and the final performance of the lattice. Direct representations of the lifetime and injection efficiency can be obtained in simulation through momentum (MA) and transverse (DA) dynamic apertures. These require to run massive tracking simulations and specific optimization algorithms.

For these studies, we have used the well-established multiobjective optimizer NSGA-II [20]. More advanced methods are now available and could be used to improve the convergence rate and gain time in future optimizations. As described in the previous sections, the LCC optics provide by design well-defined knobs aiming at tuning targeted quantities. This is the ideal configuration for such optimization work and allows to proceed in steps. The optimization of the number of turns and number of grid points with convergence studies brings the DA calculation for one case down to less than one minute. A grid of 51×51 points is used, and 256 turns are tracked for the Z lattice (32 turns for the $t\bar{t}$ lattice). The chromaticities are kept constant at the values found in Table I throughout the full optimization using the SF1 and SD1 sextupole families. The optimization is split into four main steps: (i) optimize the remaining arc sextupole families SF2 and SD2, this is done with a simple 2D scan; (ii) optimize the matching section sextupoles; (iii) optimize the final focus sextupoles (all, except for

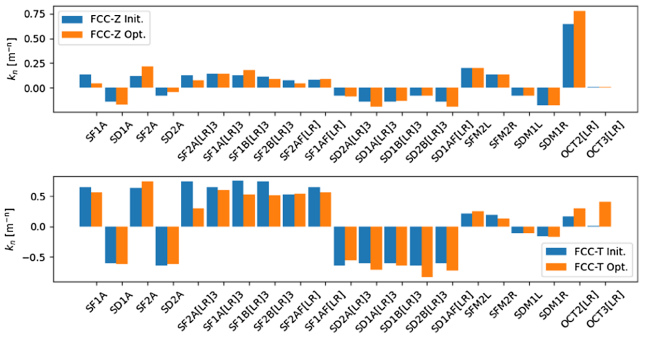

FIG. 26. Sextupole and octupole strengths before and after the optimization process for the FCC Z (top) and $t\bar{t}$ (bottom) lattices.

SF_x and SD_y); and (iv) optimize the higher order multipoles (octupoles and decapoles).

For each of these steps, the arc sextupoles can be included or not, and the magnet strength variations are kept below 40% for one optimization run.

Figure 26 shows the strengths of the sextupoles and octupoles that were varied during the optimization process. Decapoles were optimized manually on the initial lattice versions, and octupole families 0 and 1 were found to be ineffective (see Fig. 4 for their location in the final focus). These are therefore not shown in this figure. Additional sextupole families (SF_x and SD_y) are present in the final focus section of the lattice and could be used for further optimization. Multipole strengths do not increase by more than 40% except for the arc sextupoles of the FCC Z lattice with a maximum increase of 66% for the focusing sextupole family SF2A. This value nevertheless remains well below the ones of the $t\bar{t}$ lattice.

Figure 27 summarizes the results of the optimization for the FCC Z (left) and $t\bar{t}$ (right) lattices; the initial values

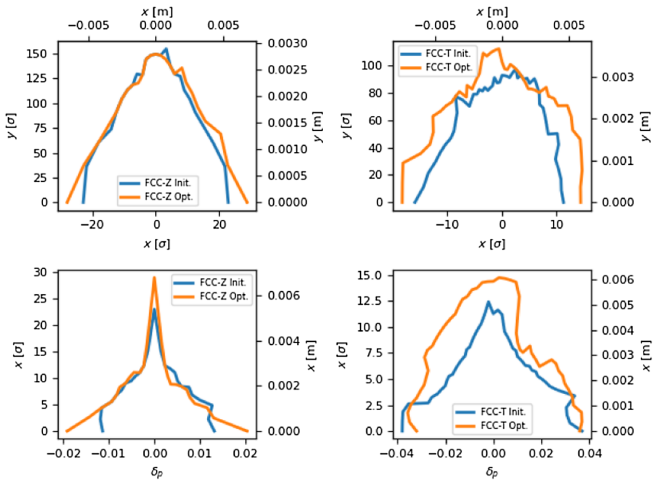

FIG. 27. Transverse and momentum dynamics aperture improvement after each optimization step for the FCC Z (left) and $t\bar{t}$ (right) lattices.

correspond to the ones obtained from the various improvements and manual optimizations presented in the previous sections. It should be noted that octupoles are stronger for the Z lattice. This does not represent a limitation, since the Z energy is the lowest and could be explained by the fact that the Z lattice design features fewer octupole families than the $t\bar{t}$ lattice design. Further tuning of the lattice design shall result in a single layout for all energies. The rf voltage is set to 170 MV and 10.4 GV for the Z and $t\bar{t}$ lattices, respectively, such that the momentum aperture is not limited by the rf acceptance and MA can be further improved by multipole optimizations. However, the optimal rf voltage operating value in collision for FCC may differ for other reasons such as beam-beam effects, collective instabilities, polarization measurement, or the maximum rf voltage available.

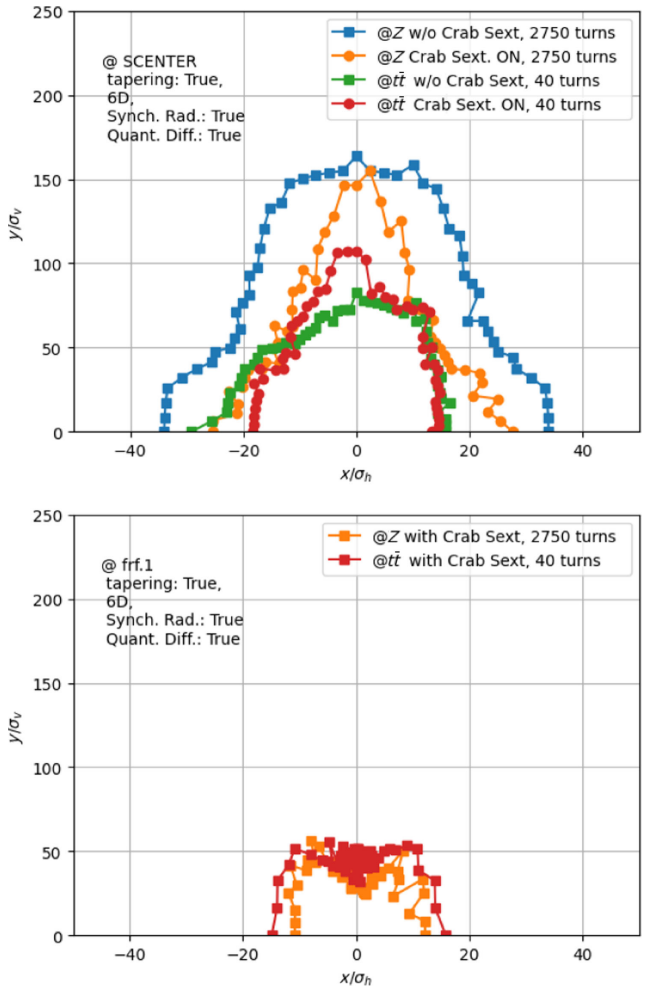

FIG. 28. Transverse dynamic aperture for FCC LCC optics (top) and GHC V22 optics (bottom) at Z and $t\bar{t}$ energy computed in the center of the straight sections. The 6D tracking for one damping time includes quantum diffusion, synchrotron radiation, and tapering. The curves with crab sextupoles use the nominal value for maximum luminosity.

It should be noted that the horizontal equilibrium emittance of the Z lattice is 0.68 nm rad, while it is 2.1 nm rad for the $t\bar{t}$ lattice. This explains the reduction of DA observed for the $t\bar{t}$ lattice when expressed in terms of beam σ. However, the absolute horizontal DA is ± 7 mm for the Z lattice and $-8/+6$ mm for the $t\bar{t}$ lattice. This should provide a sufficient margin for off-axis injection and allow for relaxed gaps in the collimation systems.

These optimizations and results were all done for an ideal lattice without errors. Introducing realistic field and alignment errors will have a strong impact on these values. However, the optimization procedure was applied to different lattices and always provided substantial improvements. It is, therefore, expected that the same method can be used to optimize lattices with errors as well as the real machine through online optimizations.

VII. LATTICE PERFORMANCE EVALUATION

Figure 28 shows the transverse dynamic aperture computed in the center of the straight sections (extreme right of Fig. 3). The 6D tracking for 2350 turns at Z and 40 turns at $t\bar{t}$ includes quantum diffusion, synchrotron radiation, tapering [21], and crab sextupoles at the optimal value for maximum luminosity. Exact Hamiltonian integrators, as described in [22], are implemented in the AT software [23] used for tracking simulations. The tracking has been benchmarked with MADX-PTC [24] tracking in [25] and shows remarkable agreement.

Always using the center of the straight sections as starting point, Fig. 29 shows the positive horizontal dynamic aperture for off-energy particles.

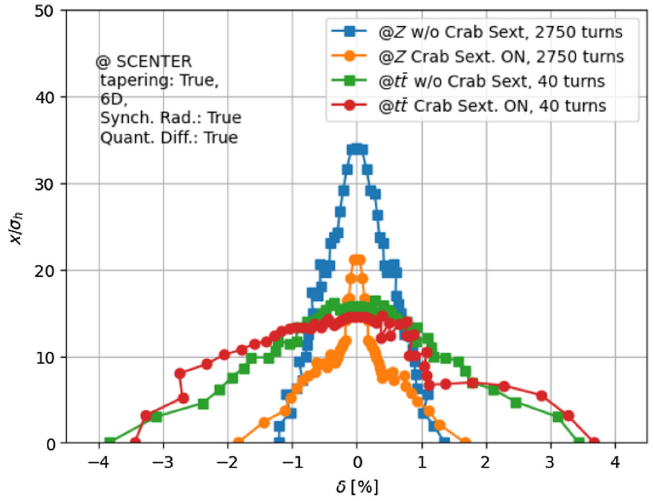

FIG. 29. Positive horizontal dynamic aperture versus energy offset for FCC LCC optics at Z and $t\bar{t}$ energy computed in the center of the straight sections. The 6D tracking for one damping time includes quantum diffusion, synchrotron radiation, and tapering. The effect of crab sextupoles at the nominal value for luminosity is shown.

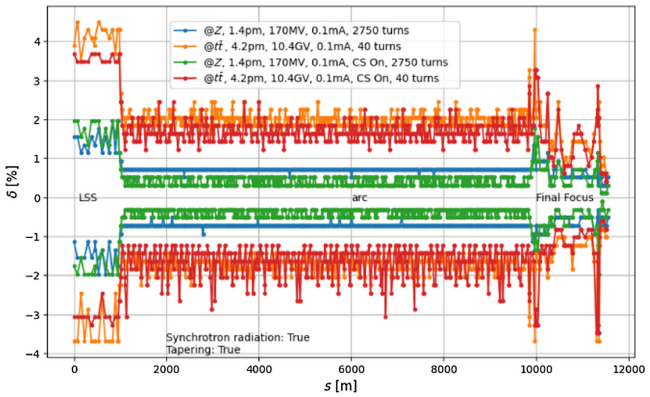

FIG. 30. Local momentum acceptance for one octant of the LCC optics at Z and at $t\bar{t}$ energies. Synchrotron radiation is not included in these simulations.

It should be noted that the momentum acceptance in general is lower in dispersive or very chromatic regions because off-energy particles will exercise simultaneously betatron and chromatic oscillations. The local momentum acceptance for one octant of the lattice is shown in Fig. 30.

VIII. SENSITIVITY TO ERRORS

The LCC lattice optics at Z and $t\bar{t}$ energies have been analyzed in terms of sensitivity to alignment errors in the arcs and the final focus. For this purpose, no corrections are applied. For each lattice optics, figures such as Fig. 31 are produced and compared. Those figures represent the evolution of β-beating, dispersion deviation, orbit, and emittances as a function of the rms amplitude of alignment errors randomly distributed in specific magnets along the ring. Tables IV (arcs) and V (FF) were compiled selecting the error values at which a given threshold was attained from plots as the one in Fig. 31. This was done for arc magnets and for the final focus magnets separately. The minimum value among horizontal and vertical alignment errors has been selected to build a more concise summary. The LCC lattice is for most parameters more tolerant or equivalent to the baseline optics [2] and to other similar lattice design such as CEPC [14].

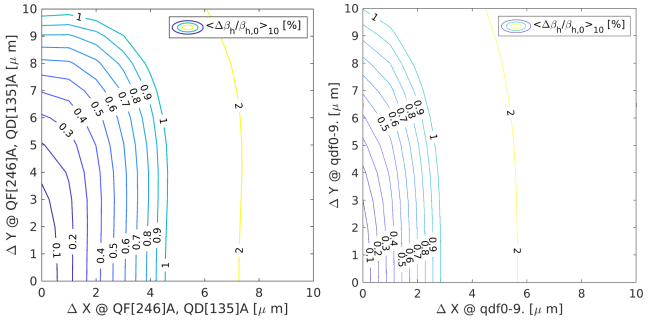

FIG. 31. Horizontal β-beating versus horizontal and vertical alignment errors on arc quardrupoles averaged at all BPMs over ten seeds without corrections. Arc quadrupoles are named QF[246]A and QD[135]A for the LCC optics and $qf[0-9]$. and $qd[0-9]$. for the GHC optics. On the left, the LCC optics, on the right plot, the GHC optics, both at Z energy.

TABLE IV. Approximate alignment sensitivity in μm for arc quadrupoles and sextupoles leading to β-beating of 1%, horizontal dispersion error of 1 mm, and vertical dispersion error of 1 mm. Tunes are (0.26 0.38) for Z and (0.224 0.36) for $t\bar{t}$. The minimum among vertical and horizontal alignment is reported. The column labeled "#" reports the number of magnets that have been misaligned for each case.

			Orbit		$\Delta\beta/\beta$		$\Delta\eta$	
			H	V	H	V	H	V
Criteria			100 μm	100 μm	1%	1%	1 mm	1 mm
Optics	E_0	#	Arc quadrupoles sensitivity (μm)					
GHC	Z	1420	1.9	1.9	2.9	0.7	0.1	0.1
LCC	Z	2168	2.0	1.6	4.5	0.38	0.8	0.25
GHC	$t\bar{t}$	2836	1.3	1.5	1.5	0.5	0.12	0.2
CEPC	$t\bar{t}$	3460	0.70	0.83	0.4	0.1	0.09	0.07
LCC	$t\bar{t}$	2168	1.4	1.0	2.1	0.41	1.2	0.32
			Arc sextupoles sensitivity (μm)					
GHC	Z	600	>100	>100	17	8.5	3.1	2.6
LCC	Z	1792	>100	>100	>100	47	14	10
GHC	$t\bar{t}$	2336	>100	>100	10	7.0	7.5	10
CEPC	$t\bar{t}$	1024	>100	>100	6.4	4.8	3.1	4.4
LCC	$t\bar{t}$	1792	>100	>100	24	12	12	12

The effect of errors in the FF is dominant, and more studies on correction schemes and tuning techniques will

TABLE V. Approximate alignment sensitivity in μm for FF quadrupoles and sextupoles leading to β-beating of 1%, horizontal dispersion error of 1 mm, and vertical dispersion error of 1 mm. Tunes are (0.26 0.38) for Z and (0.224 0.36) for $t\bar{t}$. The minimum among vertical and horizontal alignment is reported.

			Orbit		$\Delta\beta/\beta$		$\Delta\eta$	
			H	V	H	V	H	V
Criteria			100 μm	100 μm	1%	1%	1 mm	1 mm
Optics	E_0	No.	FF quadrupoles sensitivity (μm)					
GHC	Z	436	0.65	0.15	1.2	0.065	0.04	0.014
LCC	Z	532	0.57	0.11	0.63	0.035	0.18	0.018
GHC	$t\bar{t}$	480	2.0	0.35	2.1	0.25	0.23	0.08
CEPC	$t\bar{t}$	228	0.8	0.2	0.65	0.18	0.12	0.024
LCC	$t\bar{t}$	532	1.3	0.27	1.4	0.14	0.65	0.08
			FF sextupoles sensitivity (μm)					
GHC	Z	16	>10	>10	>10	0.25	>10	1.2
LCC	Z	72	>10	>10	>10	0.7	8	1.8
GHC	$t\bar{t}$	16	>10	>10	>10	0.50	>10	2.6
CEPC	$t\bar{t}$	52	>10	>10	9.5	1.3	>10	3.8
LCC	$t\bar{t}$	72	>10	>10	>10	1.6	>10	3.9

be addressed in the future to fully evaluate the tolerated alignment errors.

IX. CONCLUSIONS

HFD lattice used for FCC arcs has a very large DA and MA and very high dipole filling ratio, thus optimized energy loss per turn. Transparency conditions allow the insertion of any kind of straight section with negligible impact on DA and MA. LCC FF is a very powerful telescope with very efficient built-in compensation of high-order aberrations. LCC optic could ameliorate/alleviate many of the requirements on hardware and power consumption of FCC-ee. Machine optimization and ramp-up time might benefit as well, given the relaxed tolerances and tuning flexibility.

The HFD arc optics are very linear and arc parameters have a very large range of tunability. In addition, the horizontal emittance can be continuously varied by implementing horizontal phase advances intermediate between the Z and $t\bar{t}$ ones. HFD arcs local chromatic compensation is very beneficial in particular to reduce sensitivity to errors and stability to ground motion and temperature variations. The FF is the most aberration free telescope up to date, and it can be adopted for any circular collider. Since it has been optimized for $t\bar{t}$ operation, the left-FF could also be readily adopted for a medium energy linear collider as well, and possibly for a Tev-scale linear collider with appropriate lengthening to minimize synchrotron radiation effect. Moreover, the FF has been optimized to minimize the CS impact on DA and MA.

Arc tuning can be performed with algorithms very similar to the ones developed for synchrotron light sources [26]. The FF tuning knobs can be built very similarly to what has been developed for lepton factories such as SLC [27], NLC [28,29], LEP [30], and SuperKEKB [31,32]. The LCC optics present large orthogonality of many fundamental quantities, which can be varied separately without the need to retune other quantities: (i) arc chromaticities, (ii) machine tunes, (iii) FF chromaticities, (iv) individual IP β^*, (v) individual CS pairs, and (vi) local FF tuning knobs.

All requirements on tolerances and stability for LCC are relaxed with respect to the GHC optics design. Similarly, all requirements on magnets number and integrated strength (in particular for sextupoles) are greatly reduced. Hardware requirements for LCC optics are in line with the state of the art synchrotrons [4].

Beam dynamics optimization of the LCC optics is based on a solid and deterministic analytic approach. The detailed analysis of the effect of quadrupoles SR on beam dynamics has lead to original methods to mitigate the related DA deterioration.

Crab sextupoles detrimental effect on DA is not critical since the DA largely exceeds the requirement in [1] and its origin is clearly understood.

LCC includes all the know-how and experience acquired in designing, building, commissioning, and operating most of the high-energy and high-luminosity linear and circular colliders that have been in operation over the past 30 years. Many of the solutions developed for the last generation of synchrotron radiation sources (arc DA and MA optimization of low emittance lattices, transparency conditions) are also utilized.

DATA AVAILABILITY

The data that support the findings of this article are openly available [33].

APPENDIX A: LCC OPTICS AND MATCHING FILES

The files corresponding to the LCC optics are provided as additional files to this paper in [33]. The lattice files are provided in MAD8 [34] and AT [23] format. The matching scripts are available in MAD8 format only. The files are named `92a` for the Z optics and `92b` for the $t\bar{t}$ optics.

[1] A. Abada *et al.*, FCC-ee: The lepton collider, Eur. Phys. J. Spec. Top. **228**, 261 (2019).

[2] K. Oide *et al.*, Design of beam optics for the future circular collider e^+e^- collider rings, Phys. Rev. Accel. Beams **19**, 111005 (2016).

[3] CERN optics repository, Optics version v22 [accessed on October 14, 2024], https://acc-models.web.cern.ch/acc-models/fcc/.

[4] P. Raimondi *et al.*, The extremely brilliant source storage ring of the European synchrotron radiation facility, Commun. Phys. **6**, 82 (2023).

[5] P. Raimondi and S. M. Liuzzo, Toward a diffraction limited light source, Phys. Rev. Accel. Beams **26**, 021601 (2023).

[6] M. Bona (SuperB Collaboration), SuperB: A high-luminosity asymmetric $e^+ e^-$ super flavor factory. Conceptual design report, arXiv:0709.0451.

[7] A. Franchi, R. Tomás, and F. Schmidt, Magnet strength measurement in circular accelerators from beam position monitor data, Phys. Rev. ST Accel. Beams **10**, 074001 (2007).

[8] B. Montague, Linear optics for improved chromaticity correction (1979), LEP Notes-1979, http://cds.cern.ch/record/67243.

[9] F. Zimmermann *et al.*, Challenges for highest energy circular colliders, in *Proceedings of the 5th International Particle Accelerator Conference, IPAC-2014, Dresden, Germany* (JACoW, Geneva, Switzerland, 2014), 10.18429/JACoW-IPAC2014-MOXAA01.

[10] A. Bogomyagkov, E. Levichev, and D. Shatilov, Beam-beam effects investigation and parameters optimization for a circular e^+e^- collider at very high energies, Phys. Rev. ST Accel. Beams **17**, 041004 (2014).

[11] K. Ohmi and F. Zimmermann, FCC-ee/CepC beam-beam simulations with beamstrahlung, in *Proceedings of the 5th International Particle Accelerator Conference, IPAC'14,*

Dresden, Germany (JACoW, Geneva, Switzerland, 2014), pp. 3766–3769, 10.18429/JACoW-IPAC2014-THPRI004.
[12] S. Collaboration, SuperB technical design report, arXiv:1306.5655.
[13] Y. Ohnishi *et al.*, Accelerator design at SuperKEKB, Prog. Theor. Exp. Phys. **2013**, 03A011 (2013).
[14] The CEPC Study Group, CEPC conceptual design report: Volume 1 - ccelerator, arXiv:1809.00285.
[15] A. Louzguiti *et al.*, Optimization of the electromagnetic design of the FCC sextupoles and octupoles, IEEE Trans. Appl. Supercond. **29**, 4000805 (2019).
[16] J. Kosse, M. Koratzinos, and B. Auchmann, Reliability engineering of cryocooler-based HTS magnets for FCC-ee, IEEE Trans. Appl. Supercond. **34**, 4601505 (2024).
[17] P. Raimondi, D. N. Shatilov, and M. Zobov, Beam-beam issues for colliding schemes with large Piwinski Angle and crabbed waist, arXiv:physics/0702033.
[18] H. Wiedemann, *Particle Accelerator Physics*, 4th ed. (Springer, Berlin, 2015), 10.1007/978-3-319-18317-6.
[19] D. Shatilov, Comparison of two lattices for Z with 4 IPs, https://indico.cern.ch/event/1288750/#3-comparison-of-two-lattices-f (2023) [accessed on October 11, 2024].
[20] K. Deb, A. Pratap, S. Agarwal, and T. Meyarivan, A fast and elitist multiobjective genetic algorithm: NSGA-II, IEEE Trans. Evol. Comput. **6**, 182 (2002).
[21] S. White and L. Farvacque, Accelerator toolbox tapering method, https://atcollab.github.io/at/p/api/at.lattice.lattice_object.html#at.lattice.lattice_object.Lattice.tapering [accessed on May 28, 2024].
[22] E. Forest, *Beam Dynamics: A New Attitude and Framework*, The Physics and Technology of Particle and Photon Beams (Hardwood Academic/CRC Press, Amsterdam, The Netherlands, 1998), ISBN 978-90-5702-574-7.
[23] S. White *et al.*, Status and recent developments of python accelerator toolbox, in *Proceedings of the 14th International Particle Accelerator Conference, IPAC'23, Venice, Italy* (JACoW, Geneva, Switzerland, 2023), pp. 3185–3188, 10.18429/JACoW-IPAC2023-WEPL031.
[24] F. Schmidt, Mad-X PTC Integration, Conf. Proc. C **0505161**, 1272 (2005).
[25] S.M.Liuzzo *et al.*, Benchmark of AT vs MADX-PTC with exact integrators, in *Proceedings of the 15th International Particle Accelerator Conference, IPAC2024, Nashville, Tennessee* (JACoW, Geneva, Switzerland, 2024), MOPS09, 10.18429/JACoW-IPAC2024-MOPS09.
[26] P. Raimondi *et al.*, Commissioning of the hybrid multibend achromat lattice at the European synchrotron radiation facility, Phys. Rev. Accel. Beams **24**, 110701 (2021).
[27] N. Walker, J. Irwin, and M. Woodley, Global tuning knobs for the SLC final focus, in *Proceedings of the 15th Particle Accelerator Conference, PAC-1993, Washington, DC, 1993* (IEEE, New York, 1993), 10.1109/PAC.1993.309004.
[28] Y. Nosochkov *et al.*, Tuning knobs for the NLC final focus, in *Proceedings of the 8th European Particle Accelerator Conference, Paris, 2002* (EPS-IGA and CERN, Geneva, 2002), pp. 476–478, arXiv:physics/0206068.
[29] P. Raimondi and A. Seryi, Novel final focus design for future linear colliders, Phys. Rev. Lett. **86**, 3779 (2001).
[30] W. Wittmer, Calculating IP tuning knobs for the PEP II high energy ring using singular value decomposition, response matrices and an adapted moore penrose method, in *Proceedings of the 22nd Particle Accelerator Conference, PAC-2007, Albuquerque, NM* (IEEE, New York, 2007), pp. 3642–3644, https://jacow.org/p07/papers/THPAS068.pdf.
[31] H. Sugimoto *et al.*, Design study of the SuperKEKB interaction region optics, in *Proceedings of the 5th International Particle Accelerator Conference, IPAC'14, Dresden, Germany* (JACoW, Geneva, Switzerland, 2014), pp. 950–952, 10.18429/JACoW-IPAC2014-TUOAB02.
[32] K. Akai, K. Furukawa, and H. Koiso, SuperKEKB collider, Nucl. Instrum. Methods Phys. Res., Sect. A **907**, 188 (2018), advances in Instrumentation and Experimental Methods (Special Issue in Honour of Kai Siegbahn).
[33] P. Raimondi, S. M. Liuzzo, and S. White, LCC lattice files on Zenodo (2024), 10.5281/zenodo.13934685.
[34] F. C. Iselin and H. Grote, The MAD Program (Methodical Accelerator Design) Version 8.13/8 User's Reference Manual (1995), https://mad8.web.cern.ch/.